Journal of Luminescence 170 (2016) 736–742

Contents lists available at ScienceDirect

Journal of Luminescence

journal homepage: www.elsevier.com/locate/jlumin

Luminescence investigation of R^{3+}-doped alkaline earth tungstates prepared by a soft chemistry method

Helliomar P. Barbosa [a], Jiang Kai [b], Ivan G.N. Silva [a], Lucas C.V. Rodrigues [a], Maria C.F.C. Felinto [c], Jorma Hölsä [a,d,e], Oscar L. Malta [f], Hermi F. Brito [a,*]

[a] Instituto de Química, Universidade de São Paulo, São Paulo, SP, Brazil
[b] Pontifícia Universidade Católica do Rio de Janeiro, Departamento de Química, Rio de Janeiro, RJ, Brazil
[c] Centro de Química e Meio Ambiente, Instituto de Pesquisas Energéticas e Nucleares, São Paulo, SP, Brazil
[d] Department of Chemistry, University of Turku,FI-20014 Turku, Finland
[e] Turku University Centre for Materials and Surfaces (MatSurf), Turku, Finland
[f] Departamento de Química Fundamental, Universidade Federal de Pernambuco, Recife, PE, Brazil

ARTICLE INFO

Article history:
Received 10 February 2015
Received in revised form
9 June 2015
Accepted 13 July 2015
Available online 21 July 2015

Keywords:
Rare earths
Alkaline earth tungstate
Soft chemistry
Coprecipitation
Charge transfer
Photoluminescence

ABSTRACT

Highly luminescent rare earth (R^{3+}) doped alkaline-earth tungstates $MWO_4:R^{3+}$ (M^{2+}: Ca, Sr and Ba, R^{3+}: Eu, Tb, Gd) were prepared with a room temperature coprecipitation method. The phosphors were characterized by X-ray powder diffraction (XPD), thermal analysis (TG), infrared absorption spectroscopy (FTIR) and UV excited photoluminescence. The as-prepared $MWO_4:R^{3+}$ particles belong to the tetragonal scheelite phase, and are well crystallized and are of the average size of 16–48 nm. The excitation and emission spectra of the materials were recorded at 300 and 77 K temperatures. The luminescent materials exhibit intense red (Eu^{3+}) and green (Tb^{3+}) colors under UV excitation. The excitation spectra of the Eu^{3+} doped materials show broad bands arising from the ligand-to-metal charge transfer transitions ($O^{2-}\rightarrow W^{VI}$ and $O^{2-}\rightarrow Eu^{3+}$) as well as narrow bands from 4f–4f intraconfigurational transitions of Eu^{3+}. 4f–4f emission data of the Eu^{3+} and Tb^{3+} in the MWO_4 host matrices as well as the values of emission quantum efficiencies of the $^5D_0$ level and the 4f–4f experimental intensity parameters of Eu^{3+} ion are presented and discussed.

1. Introduction

Luminescent materials can convert photo, chemical or electrical energies into electromagnetic radiation in the ultraviolet, visible or infrared regions [1–3]. The R^{3+} doped phosphors have emerged as a class of luminescence materials, showing advantages like high photo and thermal stability, brightness, and flexible industrial processing [4]. These properties make them suitable for modern lighting devices [5], ceramics [6], polymers [7], biolabels [8], phosphors in displays [9], *etc*.

Alkaline earth tungstates MWO_4 (M: Ca, Sr and Ba) with tetragonal structure are called scheelites or stolzites [10] and exhibit blue host emission. The tungstate hosts have intense absorption bands due to Ligand-to-Metal Charge Transfer (LMCT) transitions in the near-UV region. Therefore, the tungstate compounds are strong candidates for photoluminescent systems due to the presence of allowed $O^{2-}(2p)\rightarrow W^{VI}$ transition. The Eu^{3+} and Tb^{3+} doped tungstate matrices offer new luminescent material design possibilities [11]. Moreover, tungstate luminescent materials containing Eu^{3+} and Tb^{3+} ions generally have high intense absorption bands in the UV region assigned to the LMCT and $4f^8\rightarrow 4f^7 5d^1$ interconfigurational transitions, respectively.

The traditional solid state preparation method of tungstate materials has disadvantages such as the usage of high temperature ($>1200\,^{\circ}C$) or long reaction time, high energy consumption as well as inhomogeneity of the phosphor particles and uneven distribution of particle size [12]. However, the soft chemistry methods such as sol–gel and hydrothermal methods also present issues, *e.g.* complex process, low production rate, long preparation cycle (sometimes days) and high cost of reagents [13–15]. The coprecipitation method is uncomplicated with many advantages, such as simple equipment, short reaction time and straightforward operation [16]. This procedure is environmental friendly allowing the production of materials without sacrificing sample quality and purity and, at the same time, permitting high crystallinity and control over the particle size.

* Corresponding author. Tel.: +55 11 3091 3708 fax: +55 11 3815 5579.
E-mail address: hefbrito@iq.usp.br (H.F. Brito).

http://dx.doi.org/10.1016/j.jlumin.2015.07.014
0022-2313/

In this report, the $MWO_4:R^{3+}$ nanomaterials (M^{2+}: Ca, Sr and Ba; R^{3+}: Eu and Tb) were prepared at room temperature by the coprecipitation route and their photoluminescence properties are described. The radiative and non-radiative rates (A_{rad} and A_{nrad}), experimental intensity parameters (Ω_2 and Ω_4) and experimental emission quantum efficiency (η) for the Eu^{3+} doped tungstate nanoparticles were calculated. Furthermore, the $[WO_4]^{2-}$ and Eu^{3+} LMCT states and $4f^8 \rightarrow 4f^7 5d^1$ (Tb^{3+}) transitions for these nanomaterials are discussed.

2. Experimental

2.1. Synthesis and characterization of $MWO_4:R^{3+}$ phosphors

The $MWO_4:R^{3+}$ materials were prepared with the coprecipitation method, using aqueous solution of Na_2WO_4 (99.99% Vetec), and MCl_2 [M^{2+}: $CaCl_2$ (Alfa), $SrCl_2$ and $BaCl_2$: (Synth) 99.99%]. For the preparation of $MWO_4:R^{3+}$ (10 mol%) materials, stoichiometric amounts of $MCl_2 \cdot xH_2O$ and $Na_2WO_4 \cdot 2H_2O$ all solutions (0.5 mol dm^{-3}) were separately measured. The stoichiometric amount of $RCl_3 \cdot 6H_2O$ (R^{3+}: Eu^{3+} and Tb^{3+}; 0.05 mol dm^{-3}) was added to the MCl_2 solution. The resulting solution (M^{2+} and R^{3+}) was dropwise added into the $[WO_4]^{2-}$ solution and stirred for 3 h. The materials were doped with the nominal concentrations of R^{3+} (0.1, 1.0, 5.0 and 10 mol% of the M^{2+} amount) by changing the volume and concentration of the R^{3+} solution. The white crystalline powders were washed with distilled water thrice, filtered, dried on a glass plate at 100 °C for 24 h and stored in a vacuum desiccator.

Thermogravimetric (TG) curves were obtained with a TG-50 thermobalance (Shimadzu) using platinum crucibles under a continuous synthetic air flow (50 $cm^3\ min^{-1}$) with a heating rate of 5.0 °C min^{-1}.

The infrared absorption spectra were measured using KBr pellets on a Bomem MB100 FTIR apparatus in the spectral region from 400 to 4000 cm^{-1}.

X-ray powder diffraction (XPD) patterns of the samples were registered with a Rigaku Miniflex II using $CuK_{\alpha 1}$ (1.5406 Å) radiation in the 2θ interval of 10–70° with the step of 0.02° and step measuring time of 1 s. The average crystallite sizes were estimated from the diffraction data by using the Scherrer formula [17] (Eq. (1)): where D is the average grain size (nm), λ is the X-ray wavelength (m), θ (°) is half of the Bragg angle (2θ), and β (rad) is the full width at half-maximum (FWHM) of the selected reflection. In this work, the [112] reflection (2θ: 28°) was used in the calculations. In order to correct the broadening due to the diffractometer setup $\beta^2 = \beta_s^2 - \beta_r^2$ was used where β_s and β_r are the FWHM of the material and reference (NaCl: 0.149; 31.7°; hkl: 2 0 0), respectively.

$$D_{hkl} = \frac{0.9\lambda}{\beta \cos\theta} \quad (1)$$

The photoluminescence study was conducted based on the excitation and emission spectra recorded at room temperature, using the emission measured in front face mode, with a 450 W xenon lamp as an excitation source coupled to a SPEX-Fluorolog 2 spectrometer with double emission and excitation monochromators. The emission lifetimes were investigated with a 150 W pulsed xenon lamp attached to the SPEX 1934D phosphorimeter accessory.

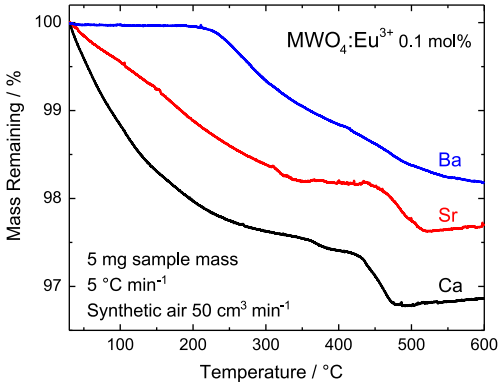

Fig. 1. TG curves of the $MWO_4:Eu^{3+}$ (M^{2+}: Ca, Sr or Ba; 0.1 mol% Eu) materials in synthetic air.

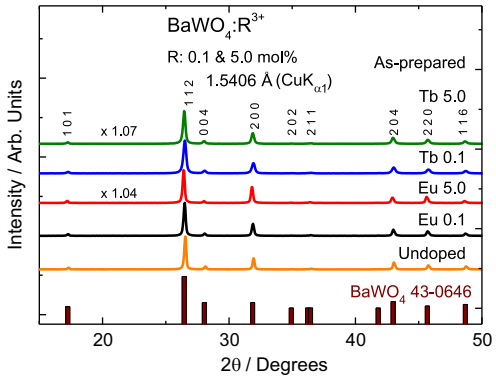

Fig. 2. The X-ray powder diffraction (XPD) patterns of the previously undoped and doped $BaWO_4:R^{3+}$ (R: Eu, Tb; 0.1 and 5.0 mol%) materials. Vertical bars at the bottom of the figure indicate the standard PDF [ICDD entry #43-0646] [19] data for the tetragonal $BaWO_4$ phase.

3. Results and discussion

3.1. Characterization

The TG curves of the $MWO_4:Eu^{3+}$ (0.1 mol%) (M: Ca, Sr and Ba) materials show a similar thermal behavior (Fig. 1). All the phosphors have a weight loss inferior to 3.0% due to adsorbed/absorbed water suggesting that the crystalline material has no phase impurities in its composition, even if the synthesis was performed in an aqueous solution. The reduction of W^{VI} is improbable.

FTIR absorption spectra of the as-prepared $MWO_4:R^{3+}$ materials exhibited weak absorption bands assigned to the O–H stretching vibrations (~3400 cm^{-1}) due to the water adsorbed by the materials and the KBr pellets (Fig. S1). The characteristic intense absorption bands assigned to the W–O symmetric stretching mode are observed at around 800 cm^{-1}. The narrow absorption bands at 400 cm^{-1} of the materials containing Ca and Sr are assigned to the δ (M–O) bending modes [18]. However, there is no corresponding absorption for $BaWO_4:R^{3+}$ materials due to higher mass ($Ca^{2+} < Sr^{2+} < Ba^{2+}$) leading to the M–O stretching at lower energy (below 400 cm^{-1}) out of the experimental range. The previously undoped and doped MWO_4 systems show similar FTIR behavior and the bands assigned to R–O stretching are absent due to low R^{3+} concentrations used.

The XPD patterns of the $MWO_4:R^{3+}$ phosphors (Figs. 2 and S2) confirm the tetragonal scheelite phase with the $I4_{1/a}$ space group (PDF entries: $CaWO_4$ 41-1431, strongest reflections: 2θ: 18.6 and 28.75, $SrWO_4$ 8-0490; 2θ: 17.9 and 27.65; $BaWO_4$ 43-0646 2θ: 26.45 and 31.9° [19]). All measured diffraction patterns of the $MWO_4:R^{3+}$ (M^{2+}: Ca, Sr and Ba; R^{3+}: Eu and Tb) materials were

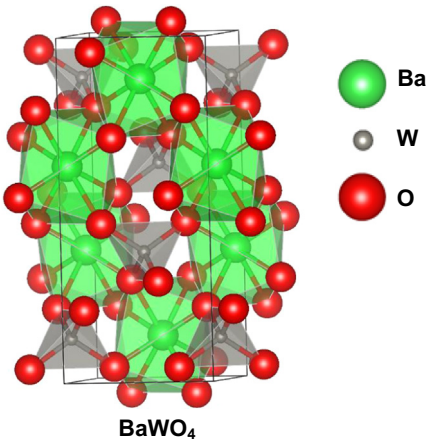

Fig. 3. A schematic VESTA [20] representation of the tetragonal structure of the $BaWO_4$ showing the tetrahedral [WO_4] and tetragonal antiprism [BaO_8]units. Structural data from [19].

indexed to a pure tetragonal scheelite phase and no additional diffraction reflections that could be attributed to impurities were observed for any matrix or for any R^{3+} concentration. The Ca, Sr and Ba ions are coordinated to eight oxygens in the tetragonal antiprism arrangement while tungsten ions are coordinated to four oxygens with the O–W–O angles slightly distorted from the tetrahedral ones (Fig. 3) [20].

Especially, no reflections originating from the $R_2(WO_4)_3$ phase were observed, indicating the efficient synthesis of the MWO_4:R^{3+} phosphors. The data also indicates the successful incorporation of R^{3+} into the host lattice due to the similar ionic radii of Eu^{3+} (1.06) and Tb^{3+} (1.04 Å) with Ca^{2+} and Sr^{2+}: 1.12 and 1.26 Å, respectively, for the coordination number 8 [21]. The Eu^{3+} ions occupy the M^{2+} site in the crystalline lattice. This difference in the ionic radii obeys the Vegard's law that establishes a limit of around 15% to obtain complete solid solubility between the dopant and the host ion [21]. Although the ionic radius of Ba^{2+} (1.42 Å, CN: 8) ion is out of this 15% range, it is still possible to observe the incorporation of Eu^{3+} in the lattice and there is no formation of another crystalline phase.

With this synthesis method, the materials showed crystallinity without phase impurities compared with the earlier reports [22–25]. The average crystallite sizes of the non-doped materials are 16 and 39 nm for $SrWO_4$ and $BaWO_4$ compounds, respectively. XPD data for the $CaWO_4$ materials were not considered, due to the overlapping reflections (112 at 28.7 and 103 at 29.0°), leading to inaccuracies in the calculation.

The crystallite sizes of $SrWO_4$ doped with 0.1, 5.0 and 10 mol% Eu^{3+} are 18, 20 and 21 nm, respectively, whereas for $BaWO_4$, the sizes are 44, 45 and 48 nm, respectively. The increasing ionic radii of the alkaline earth ion $\left(r_{Ba}^{2+} > r_{Sr}^{2+} > r_{Ca}^{2+}\right)$ may increase the crystallite size. Larger ionic radii difference between Eu^{3+} and Ba^{2+} promotes lattice distortions, leading to increased concentration of defects around the activators (Eu^{3+} and Tb^{3+}). Therefore, the crystallite size and rates of the non-radiative processes increase with subsequent decreases of luminescence efficiency [26].

The replacement of M^{2+} by R^{3+} requires charge compensation, but the ionic radii mismatch would make accommodation of R^{3+} more difficult [27]. Therefore, in solution with excess of Na^+ (from the Na_2WO_4 source), this ion enters the MWO_4:R^{3+} (M^{2+}: Ca, Sr, Ba) lattice since the size of Na^+ (1.18 Å, CN: 8) is slightly larger than that of Ca^{2+} and little smaller than Sr^{2+}. In these materials two M^{2+} sites are occupied by one R^{3+} (R^{3+}: Eu, Tb) and one Na^+ ion ensuring overall charge equilibrium compensating the charge mismatch. The entrance of Na^+ in the M^{2+} sites would decrease

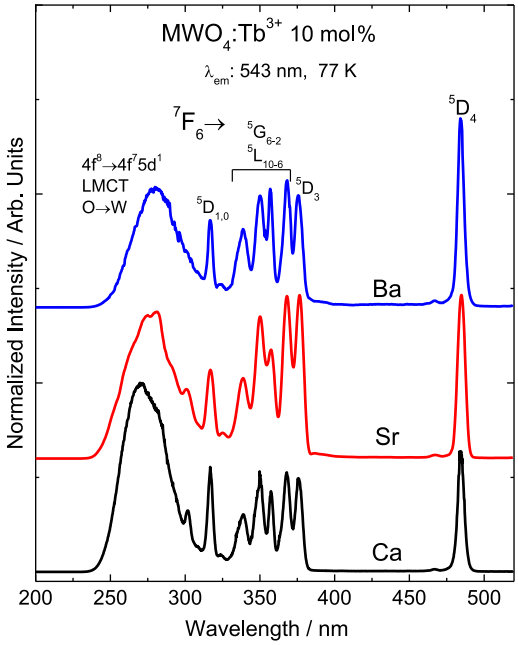

Fig. 4. The excitation spectra of MWO_4:Tb^{3+} (M: Ca, Sr, Ba; 10 mol% Tb) at 77 K.

the probability of formation of other charge compensation defects such as alkaline earth ion metal vacancies (V_M'') or interstitial oxygen (O_i'').

3.2. Photoluminescence

3.2.1. MWO_4:Tb^{3+} green emitting phosphors

The excitation spectra of the MWO_4:Tb^{3+} (10 mol%) (M^{2+}: Ca, Sr and Ba) materials were recorded monitoring the emission of the $^5D_4 \rightarrow {}^7F_5$ transition (@543 nm) of Tb^{3+} in the spectral range from 200 to 525 nm at low temperature (77 K) (Fig. 4) and exhibit similar spectral features. For comparison, the spectra at room temperature were also measured (Fig. S3).

In general, all spectra show groups of narrow absorption lines corresponding to the 4f–4f intraconfigurational transitions arising from the $^7F_6$ ground levels to (centered at the following energies in cm^{-1} units): $^5D_4$ (20,600), $^5G_6$ (26,500); $^5L_{10}$ (27,100); $^5G_5$ (27,900); $^5L_9$,$^5G_4$ (28,500); $^5L_8$,$^5L_7$,$^5L_6$,$^5G_2$ (29,100); $^5H_7$ (31,400); $^5H_6$ (33,000) and $^5H_3$,$^5F_5$ (35,300). At higher energy, the intense broad absorption bands in the range of 220–320 nm are assigned to both the O→W LMCT of the $[WO_4]^{2-}$ group and to the $4f^8 \rightarrow 4f^75d^1$ interconfigurational transitions of the Tb^{3+} ion.

In order to study the O–W LMCT transition, the excitation spectra of the Gd^{3+} doped MWO_4 materials were also measured. The Gd^{3+} ion can simulate the structural behavior of the Eu^{3+} and Tb^{3+} doped tungstate matrices owing to the similarity of their ionic radii. Besides, Gd^{3+} ion has the LMCT and $4f^7 \rightarrow 4f^65d^1$ transitions located at higher energies (> 60,000 cm^{-1}), above the LMCT and $4f^8 \rightarrow 4f^75d^1$ of Eu^{3+} and Tb^{3+}, respectively.

The excitation spectrum of the $BaWO_4$:Gd^{3+} material (Fig. 5) shows a broad absorption band centered at 265 nm (37,700 cm^{-1}) assigned to the $[WO_4]^{2-}$ LMCT transition. Based on this data, the deconvolution of the excitation spectra of the $BaWO_4$:Tb^{3+} (10 mol%) material was performed. The O→W LMCT energy was found at 34,300 cm^{-1}. In addition to this band, the energy of the $4f^8 \rightarrow 4f^75d^1$ transition was found at 32,400 cm^{-1}. The deconvolution for the other MWO_4 materials doped with Eu^{3+} and Tb^{3+} is shown in Figs. S5 and S6.

The emission spectra of the MWO_4:Tb^{3+} (10 mol%) materials were recorded at 77 K in the range of 450–700 nm under

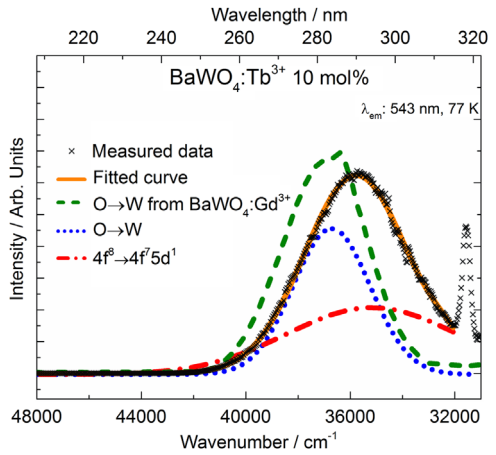

Fig. 5. The deconvolution of the excitation band of $BaWO_4:Tb^{3+}$ (10 mol%).

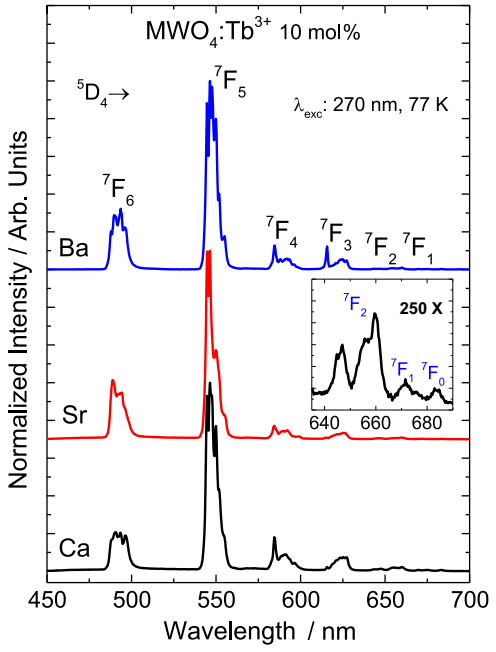

Fig. 6. The emission spectra of the $MWO_4:Tb^{3+}$ (M: Ca, Sr, Ba; 10 mol% Tb) materials under UV excitation (@ 270 nm) at 77 K.

excitation to the broad band centred at 270 nm. The spectra show narrow emission lines of from Tb^{3+} (Figs. 6 and S3) assigned to the $^5D_4 \rightarrow {}^7F_J$ transitions (barycenter given in cm^{-1}): $^7F_6$ (20,300), $^7F_5$ (18,200), $^7F_4$ (16,700), $^7F_3$ (16,100), $^7F_2$ (15,300), $^7F_1$ (14,900) and $^7F_0$ (14,700) [11,28,29]. The absence of the $^5D_3 \rightarrow {}^7F_J$ transitions is due to the non-radiative decay *via* a cross-relaxation process coupling the $^5D_3 \rightarrow {}^5D_4$ relaxation with the $^7F_6 \rightarrow {}^7F_0$ absorption that occurs with high Tb^{3+} concentrations. The broad tungstate LMCT emission band observed in $R_2(WO_4)_3$ [30] is not observed in these spectra, indicating efficient energy transfer to Tb^{3+}.

The spectra of the materials with low Tb^{3+} concentration (Fig. S7) present beside the $^5D_4 \rightarrow {}^7F_{6\text{-}0}$ transitions, a broad band attributed to the tungstate LMCT emission [29], indicating that at these low concentrations the said energy transfer process is not very efficient.

3.2.2. $MWO_4:Eu^{3+}$ red emitting phosphors

The excitation spectra (Fig. 7) of $MWO_4:Eu^{3+}$ (10 mol%) (M^{2+}: Ca, Sr and Ba) with emission monitored at 614 nm corresponding to the $^5D_0 \rightarrow {}^7F_2$ transition of Eu^{3+} exhibit all similar spectral

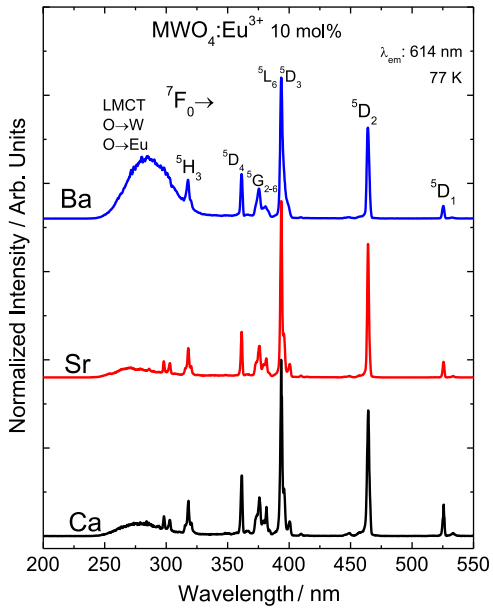

Fig. 7. The excitation spectra of the $MWO_4:Eu^{3+}$ (M: Ca, Sr, Ba; 10 mol% Eu) materials measuring the intensity of $^5D_0 \rightarrow {}^7F_2$ of Eu^{3+} (@614 nm) at 77 K.

features. They display sharp lines due to the 4f–4f transitions [30] as well as a broad band. The barycenters of the groups of narrow excitation bands in the spectral range of 310 to 590 nm originating from the $^7F_{0,1}$ state to the excited states of the Eu^{3+} ion are assigned to (in cm^{-1}): $^5F_4$ (33,400), $^5F_2$ (32,900), $^5H_3$ (31,300), $^5D_4$ (27,600), $^5L_7$ (26,200), $^5L_6$ (25,400), $^5G_{2\text{-}6}$ (25,300), $^5D_3$ (24,400), $^5D_2$ (21,500) and $^5D_1$ (19,000) [31].

The broad band in the range of 220–300 nm is assigned to two ligand–to-metal charge transfer transitions: the $O^{2-} \rightarrow Eu^{3+}$ and $O^{2-} \rightarrow W^{VI}$ [31]. Based on the Gd^{3+} doped material, as discussed in the previous section, the excitation spectra were deconvoluted (Fig. 8). The energies found for $O^{2-} \rightarrow Eu^{3+}$ (310 nm) and $O^{2-} \rightarrow W^{VI}$ (270 nm) states are in agreement with the ones reported in the literature [32,33]. The lower value of the O^{2-}–Eu energy transfer when compared to oxide compounds (*e.g.* Y_2O_3, *ca.* 260 nm [31]) is due to the effect of W^{VI}, which perturbs the $O^{2-} \rightarrow Eu^{3+}$ charge transfer. This broad CT excitation band is favorable for the effective energy transfer and luminescence of Eu^{3+}. The charge transfer (CT) band is red-shifted with increasing ionic radii of the host cation from 36,800 (Ca) and 36,400 (Sr) to 35,300 cm^{-1} (Ba) (Figs. 7 and S4). The shifts to higher energy of LMCT bands suggest that the chemical environment of the $CaWO_4$ host lattice has a stronger influence on the Eu^{3+} ion than the $SrWO_4$ and $BaWO_4$ hosts, due to the decreasing ionic radii; the ligand field around the Eu^{3+} ion should be the strongest in the $CaWO_4$ host [34–36].

The emission spectra of the $MWO_4:Eu^{3+}$ (10 mol%) (M^{2+}: Ca, Sr and Ba) materials exhibit only the $^5D_0 \rightarrow {}^7F_J$ transitions, with barycenters (in cm^{-1}) at around: $^7F_0$ (17,200), $^7F_1$ (16,800), $^7F_2$ (16,300), $^7F_3$ (15,300) and $^7F_4$ (14,300) (Figs. 9 and S4). The emission spectra show much higher intensities for the hypersensitive transitions $^5D_0 \rightarrow {}^7F_2$ than for the $^5D_0 \rightarrow {}^7F_1$ due to the absence of an inversion center in the single alkaline earth site. The $^5D_0 \rightarrow {}^7F_0$ transition gives, in all cases, only one line which is consistent with only one site being occupied by the Eu^{3+} ion.

Broadening the emission lines in the spectra of $BaWO_4:Eu^{3+}$ (Fig. 9) was observed when compared to the Ca and Sr hosts. This can be explained by the larger size of Ba^{2+} (1.42) compared to Eu^{3+} (1.06 Å), which causes off-center positions of the dopants in the Ba site, leading to a non-homogenous symmetry around Eu^{3+}.

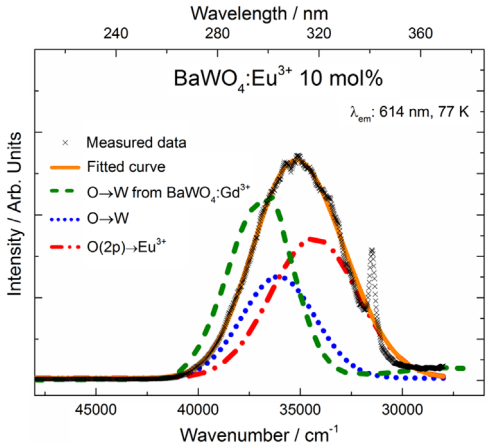

Fig. 8. The deconvolution of the LMCT bands of the $BaWO_4:Eu^{3+}$ (10 mol%) to the $O^{2-} \rightarrow W^{VI}$ and $O^{2-} \rightarrow Eu^{3+}$ LMCT bands.

The emission spectra of the materials with low Eu^{3+} concentrations (Fig. S7), similar to the Tb^{3+} case, also contain a broad band attributed to the tungstate LMCT emission [29], showing that energy transfer process to Eu^{3+} is not very efficient at low concentrations, either.

In the materials with higher concentration of Eu^{3+}, the absence of the broad emission bands in the spectral range of 350–600 nm assigned to the O→W LMCT transition, indicates that the tungstate group transfers energy efficiently to Eu^{3+}. The $MWO_4:Eu^{3+}$ materials prepared by the soft chemistry method show more operative energy transfer than those prepared by the solid state method [36], suggesting that the preparation method plays an important role in the photophysical properties of the rare earth doped tungstate materials.

The experimental intensity parameters Ω_λ (λ: 2 and 4) were determined for the $MWO_4:Eu^{3+}$ materials from the emission data recorded at room temperature. Ω_λ, also known as the Judd–Ofelt parameters, are determined by the intensities of the $^5D_0 \rightarrow {}^7F_J$ (J: 2 and 4) transitions of the Eu^{3+} ion, and the forced electric dipole and dynamic coupling mechanisms are considered simultaneously. The Einstein coefficient of spontaneous emission $A_{0\rightarrow\lambda}$, is given by [37,38] Eq. (4):

$$A_{0\rightarrow J} = \frac{4e^2\omega^3}{3\hbar c^3}\frac{1}{2J+1}\chi \sum_{\lambda=2,4,6} \Omega_\lambda \left\langle {}^5D_0 \| U^{(\lambda)} \| {}^7F_J \right\rangle^2 \quad (4)$$

where $\chi = \frac{n_0(n_0^2+2)^2}{9}$ is the Lorentz local field correction. The square of the reduced matrix elements $\langle {}^5D_0 \| U^{(\lambda)} \| {}^7F_J \rangle^2$ are obtained from [39] and the index of refraction was considered to be 1.5. The other quantities have their usual meanings. For the experimental determination of the $A_{0\rightarrow J}$ emission coefficients from the emission spectra, due to the special character of the magnetic dipole allowed $^5D_0 \rightarrow {}^7F_1$ transition was used as reference. The $A_{0\rightarrow J}$ values were obtained by using Eq. (5):

$$A_{0\rightarrow J} = A_{0\rightarrow 1}\left(\frac{\sigma_{0\rightarrow 1}}{S_{0\rightarrow 1}}\right)\left(\frac{S_{0\rightarrow J}}{\sigma_{0\rightarrow J}}\right) \quad (5)$$

where $S_{0\rightarrow\lambda}$ is the area under the curve related to the $^5D_0 \rightarrow {}^7F_\lambda$ transition obtained from the spectral data and σ_λ is the barycenter energy of the $0\rightarrow\lambda$ transition. The lifetime (τ), non-radiative (A_{nrad}) and radiative (A_{rad}) rates are related through the following equation: $A_{tot} = 1/\tau = A_{nrad} + A_{rad}$. The A_{rad} ($= \sum A_{0\rightarrow J}$) and A_{nrad} are the rates of the $^5D_0$ level. The emission quantum efficiency of the emitting $^5D_0$ level is given by Eq. (6):

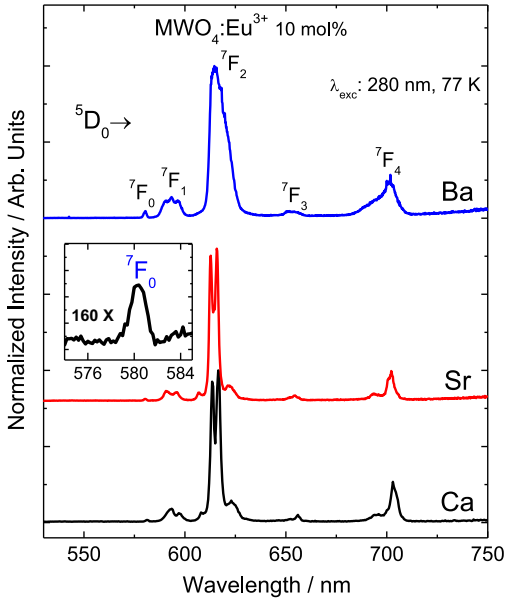

Fig. 9. The emission spectra of $MWO_4:Eu^{3+}$ (M^{2+}: Ca, Sr, Ba; 10 mol% Eu) with excitation at 270 nm at 77 K. The magnified $^5D_0 \rightarrow {}^7F_0$ transition range is for $SrWO_4:Eu^{3+}$ (10 mol%).

$$\eta = \frac{A_{rad}}{A_{rad} + A_{nrad}} \quad (6)$$

The intensity parameter Ω_2 is mostly influenced by small angular changes in the local coordination geometry. This effect, together with changes in the ligating atoms polarizabilities (α), has been used to rationalize the hypersensitive character of certain 4f–4f transitions to changes in the chemical environment. The Ω_2 and Ω_4 values for $MWO_4:Eu^{3+}$ (M^{2+}: Ca, Sr and Ba) materials (Table) are similar among the different alkaline earth ions, indicating similar chemical environment around the Eu^{3+} ion. On the other hand, there is a major increase in the parameter values with the increasing dopant concentration from 0.1 to 5 mol% as observed for the Ca host, where Ω_2 and Ω_4 increase from 7 to 15 and from 6 to 10 (in 10^{-20} cm^2 units), respectively. These higher values are due to the higher distortions caused by the high doping concentration.

The emission quantum efficiencies for $MWO_4:Eu^{3+}$ (M: Ca and Ba) are very similar ($\eta \sim 25\%$), independent of the host or concentration. On the other hand, $SrWO_4:Eu^{3+}$ materials show higher values ($\eta \sim 35\%$) (Table), suggesting that the Sr host is the most efficient among the alkaline earth tungstates.

The coordinates in the CIE (*Commission Internationale l'Éclairage*) chromaticity diagram indicate an almost pure red emission color for all $MWO_4:Eu^{3+}$ (10 mol%) materials (Fig. 10), as expected [40]. The coordinates (x, y) for the Ca, Sr and Ba hosts are (0.66, 0.33), (0.68, 0.32) and (0.69, 0.31), respectively. For the Tb^{3+} doped materials, the color coordinates are far from the green color edge due to the relatively strong intensity of the Tb^{3+} transitions in blue, yellow and even red. The green emission characteristics of the terbium doped phosphors yield the color coordinates (x, y) for the Ca, Sr and Ba hosts which are (0.30, 0.57), (0.25, 0.57) and (0.27, 0.57), respectively (Table 1).

4. Conclusions

The $MWO_4:R^{3+}$ (M: Ca, Sr and Ba; R: Eu and Tb) materials were successfully prepared by a soft chemistry coprecipitation method. This offers many advantages in comparison to conventional

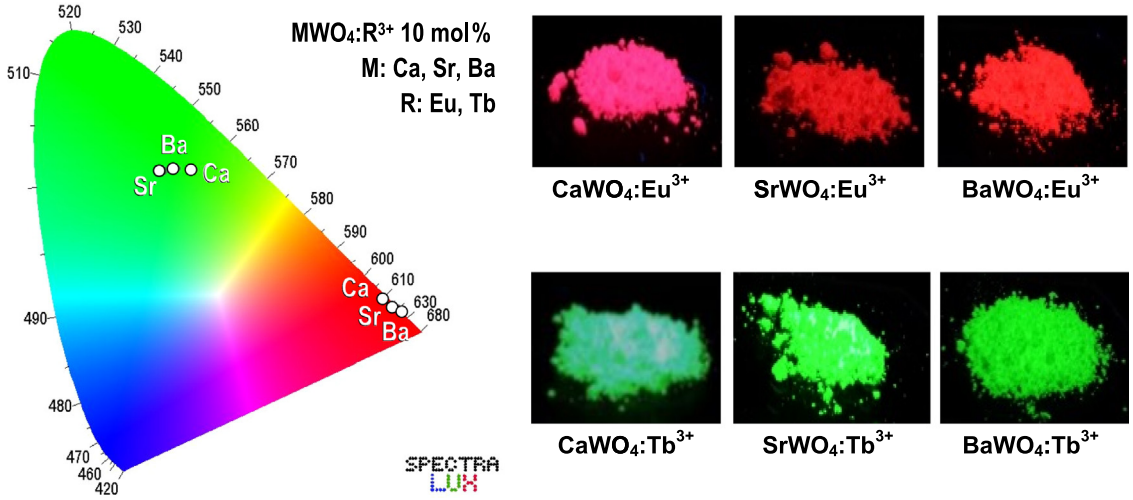

Fig. 10. The CIE chromatic diagram showing the coordinates for the $MWO_4:R^{3+}$ (M^{2+}: Ca, Sr, Ba; 10 mol% Eu, Tb). The figures are photographs of the luminescent nanomaterials taken with a digital camera displaying the red and green emissions under UV irradiation at 254 nm.

Table 1
Experimental intensity parameters (Ω_λ), radiative (A_{rad}), non-radiative (A_{nrad}) and total (A_{total}) rates, lifetimes (τ), emission quantum efficiencies (η) for the $MWO_4:Eu^{3+}$ (M^{2+}: Ca, Sr and Ba) materials, at room temperature.

$MWO_4:Eu^{3+}$ (mol%)	Ω_2 (10^{-20} cm^2)	Ω_4 (10^{-20} cm^2)	A_{rad} (s^{-1})	A_{nrad} (s^{-1})	A_{total} (s^{-1})	τ (ms)	η (%)
Ca (0.1)	7	6	356	1035	1389	0.72	25
(5.0)	15	10	652	1787	2439	0.41	27
(10)	16	11	675	1956	2632	0.38	26
Sr (0.1)	8	8	427	807	1235	0.81	34
(5.0)	14	10	636	1189	1825	0.55	35
(10)	15	13	540	1023	1562	0.64	35
Ba (0.1)	8	8	399	1243	1642	0.61	24
(5.0)	14	12	636	1902	2539	0.40	25
(10)	15	13	694	2155	2850	0.35	24

procedures, such as simple operation, low cost, fast preparation and small crystallite size. Another advantage of this synthesis is the significantly lower temperature regime than the usual solid-state method, avoiding formation of undesired phases induced by high temperatures. The Tb^{3+} doped materials exhibit very intense emission, with green color due to the prominent $^5D_4 \rightarrow {}^7F_5$ transition at around 543 nm. Under excitation at the LMCT bands, the nanostructured inorganic phosphors doped with Eu^{3+} exhibit strong red emission at 614 nm ($^5D_0 \rightarrow {}^7F_2$ transition), yielding almost pure red color. Moreover, the $MWO_4:Eu^{3+}$ materials show suitable values of emission quantum efficiencies, suggesting that the Eu^{3+} phosphors are promising candidates suitable for applications such as solid-state phosphors, optical markers, multicolor display and tunable-luminescent materials.

Acknowledgements

The authors thank the following Brazilian agencies for financial support: Conselho Nacional de Desenvolvimento Cientifico e Tecnológico (CNPq), the Coordenação de Aperfeicoamento de Pessoal de Nível Superior (CAPES), the Fundação de Amparo à Pesquisa do Estado de São Paulo (FAPESP) and inct-INAMI. One of the authors (JH) acknowledges the bilateral research programs between the Academy of Finland and CNPq (Brazil) and the Ciência sem Fronteiras (CsF) program of CNPq, as well.

Appendix A. Supplementary information

Supplementary data associated with this article can be found in the online version at http://doi:10.1016/j.jlumin.2015.07.014.

References

[1] J.-C.G. Bünzli, Chem. Rev. 110 (2010) 2729.
[2] H.A. Höppe, Angew. Chem. Int. Ed. Engl. 48 (2009) 3572.
[3] W. Strȩk, A. Bednarkiewicz, P.J. Dereń, J. Lumin. 92 (2001) 229.
[4] L.D. Carlos, R.A.S. Ferreira, V.D.Z. Bermudez, S.J.L. Ribeiro, Adv. Mater. 21 (2009) 509.
[5] S.V. Eliseeva, J.-C.G. Bünzli, Chem. Soc. Rev. 39 (2010) 189.
[6] S. Biju, R.O. Freire, Y.K. Eom, R. Scopelliti, J.-C.G. Bünzli, H.K. Kim, Inorg. Chem. 53 (2014) 8407.
[7] H. Sertchook, D. Avnir, Chem. Mater. 15 (2003) 1690.
[8] K. Binnemans, Chem. Rev. 109 (2009) 4283.
[9] Z. Wang, H. Liang, M. Gong, Q. Su, Opt. Mater. 29 (2007) 896.
[10] V. Mikhailik, H. Kraus, D. Wahl, M. Itoh, M. Koike, I. Bailiff, Phys. Rev. B69 (2004) 205110.
[11] B.C. Grabmaier, J. Lumin. 60 (61) (1994) 967.
[12] A.M. Kaczmarek, R. Van Deun, Chem. Soc. Rev. 42 (2013) 8835.
[13] Y. Pan, Q. Zhang, C. Zhao, Z. Jiang, Solid State Commun. 142 (2007) 24.
[14] Z. Hou, C. Li, J. Yang, H. Lian, P. Yang, R. Chai, Z. Cheng, J. Lin, J. Mater. Chem. 19 (2009) 2737.
[15] Z. Hou, Z. Cheng, G. Li, W. Wang, C. Peng, C. Li, P. Ma, D. Yang, X. Kang, J. Lin, Nanoscale 3 (2011) 1568.
[16] Q. Zhang, Q. Meng, W. Sun, Opt. Mater. 35 (2013) 915.
[17] H.P. Klug, L.E. Alexander, X-Ray Diffraction Procedures for Polycrystalline and Amorphous Materials, 2nd ed., Wiley, New York, 1974.
[18] T. Thongtem, A. Phuruangrat, S. Thongtem, Appl. Surf. Sci. 254 (2008) 7581.
[19] The International Centre for Diffraction Data – ICDD, Entries 41–1431 $CaWO_4$, 8–0490 $SrWO_4$, and 43–0646 $BaWO_4$, 72-0504: $Eu_2(WO_4)_3$ and 28-1290: $Tb_2(WO_4)_3$, 1997.
[20] K. Momma, F. Izumi, J. Appl. Crystallogr. 41 (2008) 653.
[21] R.D. Shannon, Acta Crystallogr. A32 (1976) 751.
[22] P.S. Dutta, A. Khanna, ECS J. Solid State Sci. Technol. 2 (2012) R3153.
[23] A. Khanna, P.S. Dutta, J. Solid State Chem. 198 (2013) 93.
[24] J.H. Ryu, J.-W. Yoon, K.B. Shim, Electrochem. Solid-State Lett. 8 (2005) D15.
[25] A. Phuruangrat, T. Thongtem, S. Thongtem, Superlattices Microstruct. 52 (2012) 78.
[26] I.K. Battisha, A. Speghini, S. Polizzi, F. Agnoli, M. Bettinelli, Mater. Lett. 57 (2002) 183.
[27] J. Hölsä, T. Laamanen, M. Lastusaari, M. Malkamäki, J. Niittykoski, P. Novák, Radiat. Phys. Chem. 78 (2009) S11.
[28] C.A. Kodaira, H.F. Brito, E.E.S. Teotonio, M.C.F.C. Felinto, O.L. Malta, G.E.S. Brito, J. Braz. Chem. Soc. 15 (2004) 890.
[29] C.A. Kodaira, H.F. Brito, O.L. Malta, O.A. Serra, J. Lumin. 101 (2003) 11.
[30] C.A. Kodaira, H.F. Brito, M.C.F.C. Felinto, J. Solid State Chem. 171 (2003) 401.
[31] I.G.N. Silva, L.C.V. Rodrigues, E.R. Souza, J. Kai, M.C.F.C. Felinto, J. Hölsä, H. F. Brito, O.L. Malta, Opt. Mater. 40 (2015) 41.
[32] B. Grobelna, P. Bojarski, J. Non, Cryst. Solids 355 (2009) 2309.
[33] Q. Meng, R. Hua, B. Chen, Y. Tian, S. Lu, L. Sun, J. Nanosci. Nanotechnol. 11 (2011) 182.
[34] N. Li, S. Zhang, J. Phys. Chem. B110 (2006) 21438.

[35] J. Liao, B. Qiu, H. Wen, J. Chen, W. You, L. Liu, J. Alloy. Compd. 487 (2009) 758.
[36] F. Kang, Y. Hu, L. Chen, X. Wang, H. Wu, Z. Mu, J. Lumin. 135 (2013) 113.
[37] L.U. Khan, H.F. Brito, J. Hölsä, K.R. Pirota, D. Muraca, M.C.F.C. Felinto, E.E. S. Teotonio, O.L. Malta, Inorg. Chem. 53 (2014) 12902.
[38] G.F. de Sá, O.L. Malta, C. de Mello Donegá, A.M. Simas, R.L. Longo, P.A. Santa-Cruz, E.F. da Silva, Coord. Chem. Rev. 196 (2000) 165.
[39] W.T. Carnall, H.M. Crosswhite, Energy Level Structure and Transition Probabilities in the Spectra of the Trivalent Lanthanides in LaF_3, Argonne, IL (United States), 1978.
[40] P.A. Santa-Cruz, F.S. Teles, Spectra Lux Software v.2.0 Beta, Ponto Quântico Nanodispositivos, RENAMI, UFPE, Recife-PE, Brazil, 2003.